5

Utilization of Nanoparticles Produced by Aqueous-Solution Methods – Formation of Acid Sites on CeO_2-TiO_2 Composite and 1-D TiO_2 for Dye-Sensitized Solar Cells

Motonari Adachi et al.*
Fuji Chemical Co., Ltd., 1-35-1 Deyashikinishi-Machi, Hirakata, Japan

1. Introduction

Nanoparticles with well-defined nanostructures with unique physical properties are assembled into optoelectronic (Colvin et al. 1994), and nano electronic (Fuhrer et al. 2000) devices and other functional materials (Morris et al. 1999). Highly crystallized nanoparticles can be produced by aqueous-solution methods which provide low cost and ease of fabrication.

In this chapter two utilizations of nanoparticles are presented. First one is formation of acid sites on CeO_2-TiO_2 composite. Cerium dioxide has an unusual ability to shift easily between the reduced and oxidized states ($Ce^{3+} \rightleftarrows Ce^{4+}$). This ability coupled with a high oxygen transport capacity gives a unique property of catalysis. Based on the remarkable properties of cerium dioxide, catalytic activity of nanoscale composite of CeO_2-TiO_2 was studied with variation in composition and formation temperature, which brought change in the number of Lewis acid site together with morphological changes.

The second one is 1-D TiO_2 for dye-sensitized solar cells (DSSCs). We succeeded in the preparation of titania nanorods (Jiu et al. 2006), network structure of titania nanowires (Adachi et al. 2004) and one-dimensional titania nanochains. All cells composed of these highly crystallized 1-dimensional titania nanoscale materials (1DTNM) show high power

* Keizo Nakagawa[2], Yusuke Murata[3], Masahiro Kishida[4], Masahiko Hiro[5], Kenzo Susa[6], Jun Adachi[7], Jinting Jiu[8] and Fumio Uchida[1]
[1]*Fuji Chemical Co., Ltd., 1-35-1 Deyashikinishi-machi, Hirakata, Japan*
[2]*Department of Advanced Materials, Institute of Technology and Science, The University of Tokushima, Minami-josanjima, Tokushima, Japan*
[3]*Toyo Tanso Co., Ltd., 5-7-12 Takeshima, Nishiyodogawa-ku, Osaka, Japan*
[4]*Graduate School of Engineering, Kyushu University,744 Motooka, Nishi-ku, Fukuoka, Japan*
[5]*Hitachi Chemical Co., Ltd., 2-1-1 Nishishinjuku, Shinjuku, Tokyo, Japan*
[6]*Trial Corporation., 2-195 Asahi, Kitamoto, Japan*
[7]*National Instituite of Biomedical Innovation, 7-6-8 Asagi Saito, Ibaraki, Japan*
[8]*The Institute of Scientific and Industrial Research (ISIR), Osaka University, 8-1 Mihogaoka, Ibaraki, Japan*

conversion efficiency about 9 %. We also present necessity of 1DTNM for attainment high efficiency theoretically based on the consideration of electron transport processes in the titania electrode and then present that it is indispensable to use highly crystallized 1DTNM for attainment of higher efficient DSSCs based on the analysis of experimental results obtained by electrochemical impedance spectroscopy (EIS) and I−V measurements.

2. CeO_2-TiO_2 composite as a catalyst

Ceria-based materials are major compounds of the rare earth family, and these have been extensively studied and found application as ultraviolet absorbers (Masui et al., 1997, 2000), solid electrolytes (Inaba & Tagawa, 1996), so-called three-way catalysts for automotive exhaust catalysts (Bekyarova et al., 1998), and soot oxidation catalysts (Pisarello et al., 2002; Aneggi et al., 2006). Nanocrystalline ceria materials have received much attention owing to their physical and chemical properties, which are markedly different from those of the bulk materials. Of particularly interest, the electronic conductivity of CeO_2 can be enhanced four orders of magnitude when its microstructure is changed from the micro- to nanocrystalline region (Chiang et al., 1996). Various aqueous solution-based methods for synthesizing crystallized CeO_2 nanoparticles (Masui et al., 2002a; Hirano et al., 2000; Li et al., 2001; Wu et al., 2002; Zhou et al., 2003; Bumajdad et al., 2004) and 1D, 2D and 3D CeO_2 nanostructures with different morphologies (Vantomme et al., 2005, Zhou et al., 2005, Kuiry et al., 2005, Ho et al., 2005; Han et al., 2005; Sun et al., 2006; Zhong et al., 2007) have been investigated. Some of the properties of these materials, such as the dispersibility of the particles (Masui et al., 2002a) and their catalytic properties (Masui et al., 1997; Sun et al., 2006; Zhong et al., 2007) have also been studied.

The features of CeO_2 in these applications are mainly due to the unique combination of its elevated oxygen transport capacity, coupled with its ability to shift easily between the reduced and oxidized states ($Ce^{3+} \leftrightarrow Ce^{4+}$). To increase the temperature stability and ability of ceria to store and release oxygen, other transition and non transition metal ions (such as Al^{3+}, Si^{4+}, Ti^{4+} and Zr^{4+}) are normally introduced into the ceria cubic structure (Reddy et al., 2003, 2005; Rynkowski et al., 2000; Masui et al., 2002b). The redox and catalytic properties of CeO_2 are strongly influenced when it is combined with other transition metals. In addition, when the particle size is decreased below 100 nm, the materials become nanophasic, where the density of defects increases, such that up to half (50%) of the atoms are situated in the cores of the defects, promoting fast catalyst activation and reaction kinetics (Reddy et al., 2005). Thus, a study of the synthesis and reaction characteristics of nano-sized ceria-based mixed oxides is very important for utilizing the oxygen transport capacity and redox properties. One of the main disadvantages of ceria-based nanoparticles prepared in aqueous solution, however, is the resultant hard agglomeration of the fine particles, which has posed a major challenge to the realization of the full potential of nanocrystalline CeO_2 powders.

In this section, first we present the preparation of cubic CeO_2 nanoparticles using an alkoxide-primary amine surfactant in an aqueous solution and the existence of a clear potential to make 1D, 2D or 3D CeO_2 materials by assembling cubic-shape CeO_2 nanoparticle building blocks. Amine surfactant works as a colloidal stabilizer through the adsorption on the CeO_2 nanoparticles. Second, the preparation of CeO_2-TiO_2 nanocomposite nanostructures is presented. The morphologies and redox reactivities of CeO_2-TiO_2

composite nanostructures are influenced by changing the mole ratio of cerium/titanium alkoxides and by changing the calcination temperature.

2.1 Preparation of CeO_2 nanoparticles and CeO_2-TiO_2 composite nanostructure

The preparation method of CeO_2 nanoparticles and CeO_2-TiO_2 composite are based on the aqueous solution system including metal alkoxides and amine surfactant molecules. The experimental procedure has been described in detail in our previous papers (Murata & Adachi, 2004; Nakagawa et al., 2007). The typical synthesis was as follows: first, laurylamine hydrochloride (LAHC) was dissolved in distilled water. Cerium tri-isopropoxide (CTIP) or cerium *n*-butoxide (CeBu) was used as a cerium source. Tetraisopropyl orthotitanate (TIPT) was used as a titanium source. In the synthesis of CeO_2 nanoparticles, CTIP or CeBu was mixed with acetylacetone (ACA) in a beaker and immediately added to an aqueous LAHC solution at pH 4.6. In the case of the synthesis of CeO_2 – TiO_2 composite nanostructures, the mole ratio of CeBu to TIPT (CeBu/TIPT) was changed to 100/0, 75/25, 25/75 and 0/100. Each mixed alkoxide solution was mixed with acetylacetone. In all cases, the mole ratio of metal alkoxides to ACA and metal alkoxides to LAHC were 1 and 4, respectively. After stirring at room temperature for 1 h, the reaction temperature was then changed to 353 K. When the two solutions were mixed, precipitation occurred immediately. After 1 week, the precipitates were separated by centrifugation. After washing with 2-propanol and successive centrifugation, the obtained products were dried through a combination of freeze-drying and vacuum drying, and calcined in air at different temperatures.

2.2 Cubic CeO_2 nanoparticles and their assembled structures

The formation yield of CeO_2 particles for the surfactant assisted-process was 100% approximately. The structure of CeO_2 nanoparticles was studied by TEM image of CeO_2 sample in a dried state. During the formation process, we observed systematic changes in color of the precipitated particles. After mixing of the solution of CTIP or CeBu modified with ACA with the aqueous solution of LAHC, the brown transparent original solution immediately became dark brown. The white colloidal suspension was formed after stirring for 1 h at room temperature. A brown and clear supernatant was formed after the precipitation. Further color change of the precipitate was observed. First, the color of the CeO_2 particles changed from white to dark blue in about 1 day at 353 K. Subsequently, the color of the precipitate gradually turned into pale purple for 1 week, but the color change was slower than the first change. Moreover the wet centrifuged precipitate appeared dark blue, and the freeze-dried powders were gray. But final CeO_2 particles calcined at 673 K was light yellow. These changes in color were observed in the cases that the particles were synthesized in LAHC surfactant aqueous solution at pH 4.2. On the other hand, there was no color change of the precipitate without LAHC surfactant. These color changes are related to the valence state of the Ce; most likely purple corresponds to Ce^{3+} and yellow corresponds to Ce^{4+}. Therefore, it is clear that the Ce^{3+} oxide is stabilized by existence of LAHC in aqueous solution.

We succeeded in the preparation of CeO_2 nanoparticles with cubic structures and 1D, 2D or 3D CeO_2 nanostructures by assembling the cubic-shape CeO_2 nanoparticle building blocks (Murata & Adachi, 2004, Nakagawa et al., 2007) as shown in Fig. 1, 2 and 3. It is evident

from this figure that the particle shape was square, and the particle size was calculated to be 2.7-3.8 nm. Furthermore, it seems that the particles were aligned. TEM image of Figure 1a clearly showed the mono-dispersed CeO_2 nanoparticles. The inset picture shows the SAED pattern and Debye-Scherrer rings of the nanoparticles, which can be indexed as those of cerium oxide with the cubic fluorite structure. The HRTEM images and FFT pattern as shown in Figure 1b show that the CeO_2 cubic nanoparticles had a single crystalline structure and high crystallinity; these lattice images were observed for many particles. The main lattice spacing of the crystalline structure was calculated to be 3.11 Å according to FFT analysis. This lattice spacing corresponds to the (111) planes of CeO_2 with a cubic phase, which coincides with the SAED analysis.

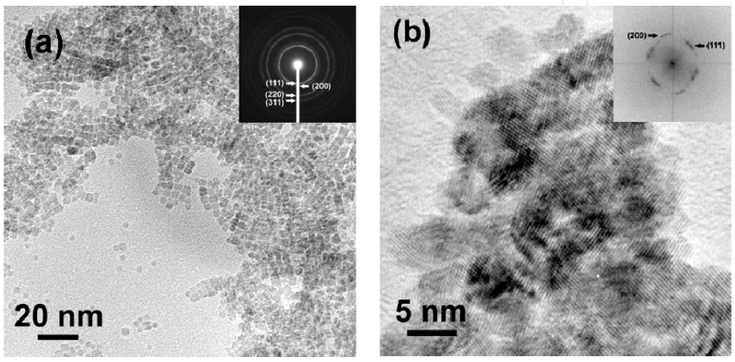

Fig. 1. (a) Low-magnification TEM images of the freeze-dried CeO_2 nanoparticles prepared at 353 K for 1 week. Inset: SAED pattern. (b) High-Resolution TEM images of the aggregated CeO_2. The lattice images were observed. Inset: FFT pattern obtained from HRTEM.

1D rod-like CeO_2 structures are obtained after calcination at 673 K. Rod-like CeO_2 with diameters of 30 nm and lengths of 180 nm are observed although the majority of CeO_2 samples were assembled into aggregates as shown in Fig.2. The HRTEM image show that the principal axis of the crystal growth of CeO_2 was aligned along the rod axis.

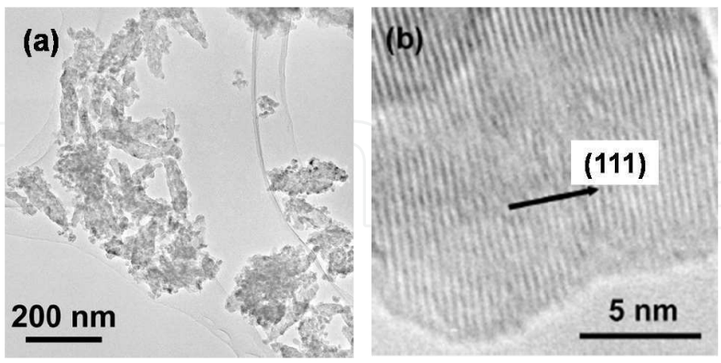

Fig. 2. (a) TEM images of CeO_2 calcined at 673 K for 4 h. (b) HRTEM image of rod-like CeO_2 with a clearly lattice image of (111) planes (d = 3.11 Å).

An ordered structure (2D or 3D superlattice-like structure) are also obtained from the freeze-dried CeO_2 nanoparticles. Figure 3 shows an array of cubic nanocrystals with a mean inter-particle (center-to-center) distance of 2.9 nm, as determined from direct imaging and the FFT pattern. We believe this assembly with an ordered structure is formed to minimize the total

surface energy, which is attained by the association of the cubic CeO_2 with a face-to-face structure.

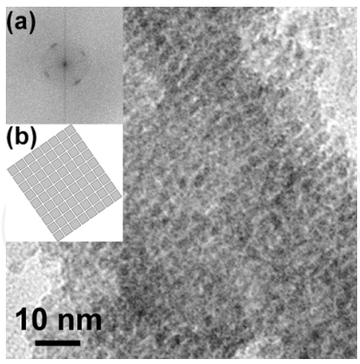

Fig. 3. TEM image of CeO_2 nanocrystals self-assembled into a superlattice-like arrangement with dimensions of the order on the nano-scale, Inset a: the FFT pattern confirms the orientational order of the superlattice-like structure, Inset b: the model structure demonstrates the superlattice-like assembled CeO_2 nanoparticles.

The thermodynamics of hydrolysis and condensation depend on the strength of the entering nucleophile and electrophilicity of the metal, and on the partial charge. Transition metals are very electropositive, and the hydrolysis and condensation kinetics of the transition metal alkoxides are affected by the positive partial charge δ^+ (Livage et al., 1988). Positive partial charge δ^+ for metals in various alkoxides have been reported; for example, cerium alkoxide: 0.75, titanium alkoxides: 0.63, and silicon alkoxides: 0.32. Since a large positive partial charge corresponds to a rapid reaction rate, the precursor for the complex formed from cerium alkoxide was not generated gradually, but the nano-sized particles were formed by the rapid hydrolysis and condensation reactions. In our systems using LAHC and CTIP (or CeBu) modified with ACA, the resulting suspensions of CeO_2 nanoparticles were exceptionally mono-dispersive without aggregation, demonstrating the high power of LAHC as a colloidal stabilizer through the adsorption of LAHC on the surface of the CeO_2 nanoparticles, in accordance with the results of Sugimoto et al. who reported the effect of primary amines as shape controllers for the synthesis of TiO_2 (Sugimoto et al., 2003). Since the shape of the CeO_2 particles is nearly cubic even if the cubic shape has somewhat rounded edges and corners, the LAHC would control the morphology of the CeO_2 particles.

For hydrous oxides in aqueous solution systems, the charge-determing ions are H^+ and OH^-, which establish the charge on the particles by protonating or deprotonating the MOH bonds on the surface of the particles.

$$M\text{-}OH + H^+ \rightarrow M\text{-}OH_2^+ \quad (1)$$

$$M\text{-}OH + OH^- \rightarrow M\text{-}O^- + H_2O \quad (2)$$

The ease of protonation and deprotonation on the surface of the oxide depends on the metal atom. The pH at which the particle is neutrally charged is called the point of zero charge (PZC). At pH > PZC, Eq. 2 predominates, and the particle is negatively charged, whereas at pH < PZC, Eq.1 makes the particle positive. Value of the PZC for CeO_2 particles is 8.1 (De Faria and Trasatti, 1994). The magnitude of the surface potential depends on the departure

of the pH from the PZC, and that potential attracts oppositely charged ions that present in the solution. Therefore, at pH 4.2, the hydrolyzed and condensed CeO_2 particle is positively charged. LAHC molecules also have a positively charged amine group under acidic condition. Hence, there seems to be no driving force for adsorption by electrostatic attraction. However, chloride ion (Cl^-) mediates the interaction between the laurylamine surfactant and charged CeO_2 by weak H-bonding forces, and CeO_2 particles are covered by surfactant molecules, resulting in the formation of cube crystals. Since the adsorption of LAHC takes place to a specific crystal face, anisotropic structures such as cubes would be formed.

2.3 Morphology of CeO_2-TiO_2 composite

A few studies on CeO_2 – TiO_2 composite nanoparticles (Reddy et al., 2003, 2005; Rynkowski et al., 2000; Masui et al., 2002b) have been reported. Reddy et al. obtained CeO_2 – TiO_2 composites comprised of relatively larger nanocrystals of CeO_2 and TiO_2 (anatase), and some overlapped regions (Reddy et al., 2005). Rynkowski et al. studied the redox properties of CeO_2 – TiO_2 composites (Rynkowski et al., 2000), and stated the existence of the CeO_2 – TiO_2 composite. Masui et al. also synthesized CeO_2 – TiO_2 composite nanoparticles, and reported the deactivation of the thermal and photocatalytic properties of this species by the formation of the CeO_2 – TiO_2 composite (Masui et al., 2002b).

We also studied the preparation of CeO_2-TiO_2 composite nanostructures by changing the mole ratio of cerium/titanium alkoxides and found the effective redox reactivities of CeO_2-TiO_2 composite nanostructures (Nakagawa et al., 2007). During the synthesis of CeO_2-TiO_2 composite, the reaction behavior of each solution was observed. When the surfactant solution and metal alkoxide solutions were mixed, precipitation occurred immediately. When the mole ratio of CeBu/TIPT = 75/25 and 25/75, dark brown-gels and dark purple-precipitates formed, while purple-precipitates with a transparent liquid layer were observed at the mole ratios of CeBu/TIPT = 100/0, that was the same behavior using CTIP. The morphology and crystalline structure of the CeO_2-TiO_2 composite nanostructures varied according to the change in the mole ratio of CeBu to TIPT. When CeBu/TIPT was 75/25, the nano-network structure with a diameter of 3–9 nm was observed and the SAED pattern indicated a cubic fluorite structure (Figure 4). Whereas, when CeBu/TIPT was 25/75, aggregate structures of rod-like morphology with an average diameter of 20 nm and length of 80 nm were observed, and the SAED pattern showed several spots corresponding to the lattice plane of the anatase phase of TiO_2 (Figure 5). In the case of the synthesis with only TIPT, a TiO_2 nano-network structure of connecting nanowires with diameter of 5–15 nm formed by an oriented attachment mechanism (Adachi et al., 2004, Nakagawa et al., 2005).

Figure 6 shows the variation in XRD patterns of the CeO_2-TiO_2 composite calcined at 673 K for 4 h (Nakagawa et al., 2007). The peaks at CeBu/TIPT = 100/0 are sharp and can be indexed to a CeO_2 cubic fluorite structure. When CeBu/TIPT was 75/25, the XRD peaks were indexed to a CeO_2 cubic fluorite structure, although the peaks became very broad. The reason for the broad peak is due to the formation of composite materials. In the HRTEM image shown in Figure 4b, the lattice image of the (111) plane of the cubic fluorite structure could be observed. These observations indicate that the crystalline structure of the nano-network at CeBu/TIPT = 75/25 consists of a CeO_2 cubic fluorite structure, which is different

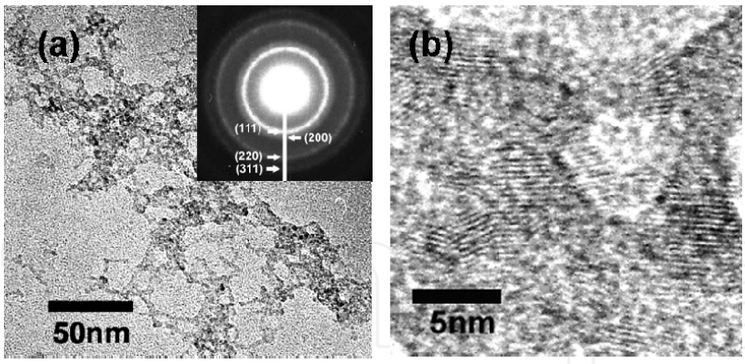

Fig. 4. (a) TEM and (b) HRTEM image of CeO_2 – TiO_2 composite nanostructures (CeBu/TIPT = 75/25) after reaction at 353 K for 1 week, inset: SAED patterns.

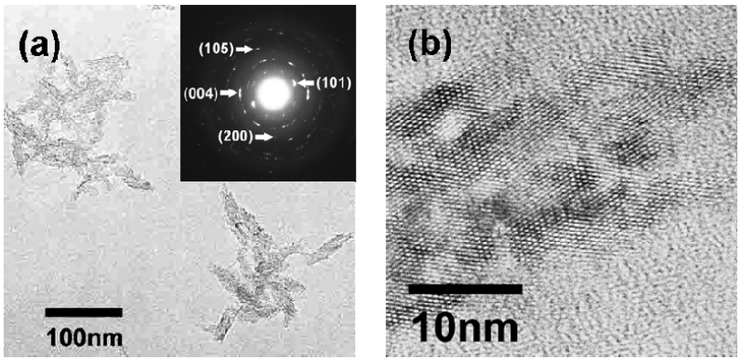

Fig. 5. (a) TEM and (b) HRTEM image of CeO_2 – TiO_2 composite nanostructures (CeBu/TIPT = 25/75) after reaction at 353 K for 1 week, inset: SAED patterns.

from that of pure CeO_2. No TiO_2 anatase peaks were observed. Therefore, the formed materials under CeBu/TIPT = 75/25 constitute the composite materials of CeO_2 and TiO_2, i.e., the formed materials are not a simple mixture of pure CeO_2 and TiO_2. As a characteristic of our reaction system, the initial solution, including the two metal alkoxides is uniformly well mixed on a molecular scale, easily leading to the formation of composite materials. Since the positive partial charge δ^+ of cerium alkoxide is larger than that of titanium alkoxide, as mentioned above, it is inferred that the reaction rate of CeBu is faster than TIPT. Moreover, the content of cerium is much higher than titanium. From these facts, the crystalline structure of the composite materials is inferred as a CeO_2 cubic fluorite structure, which is different from that of pure CeO_2. The different crystalline structure creates a new morphology, i.e., a nano-network structure, which also leads to the formation of Lewis acid sites, as described later. The XRD patterns at CeBu/TIPT = 25/75 show mainly broad peaks of the TiO_2 anatase phase and also show a broad peak of CeO_2 around $2\theta = 30^\circ$. The broad peaks indicate the formation of composite materials, which lead to a nanorod structure. Since the content of titanium is much higher than cerium, the main crystalline structure corresponds to the TiO_2 anatase phase, but a small amount of CeO_2 crystalline structure is also included, because the reaction rate of CeBu is faster than TIPT.

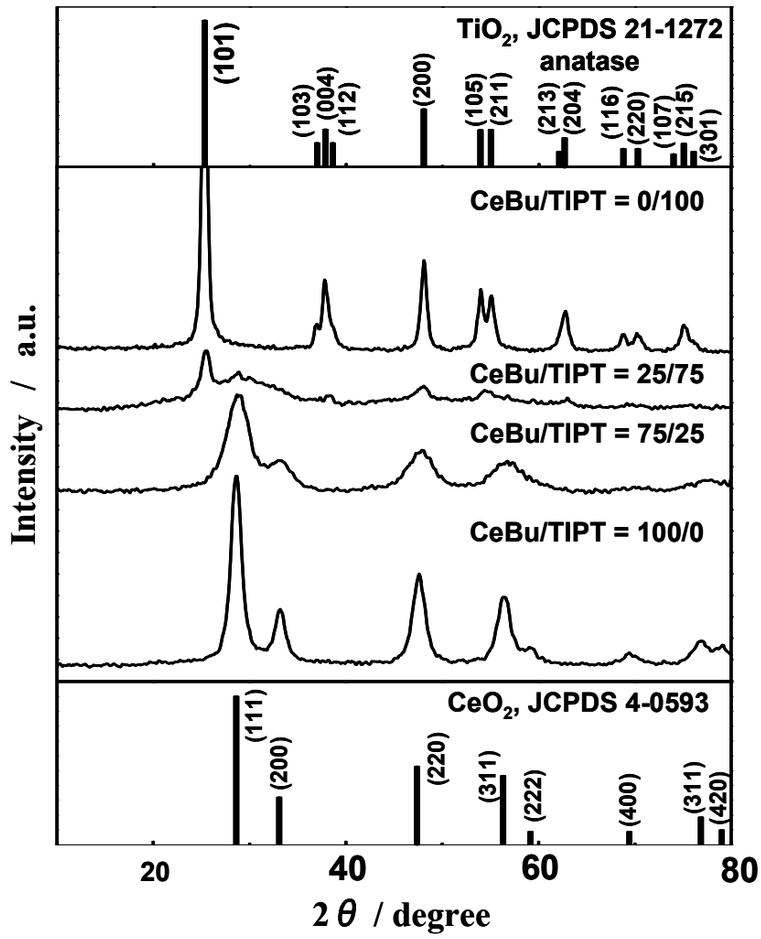

Fig. 6. XRD patterns of the CeO_2–TiO_2 composite nanostructures at the mole ratio of CeBu/TIPT = 100/0, 75/25, 25/75 and 0/100 after calcination at 673K for 4 h.

2.4 Surface properties of CeO_2-TiO_2 composites

The reaction activity of CeO_2-TiO_2 composite nanostructures was investigated through the formation rate of I_3^-, formed due to the oxidation of I^- to I_2 in excess KI aqueous solution (Nakagawa et al., 2007). Nanostructured CeO_2-TiO_2 (10 mg) was suspended by magnetic stirring in 10 ml of 0.2 M KI aqueous solution without light irradiation. After initiation of the reaction, 0.3 ml of the reaction solution was taken, and the concentration diluted to one tenth. The concentration of I_3^- was measured using a Shimadzu UV-2450 spectrometer from the absorbance at 288 nm. Figure 7 shows the I_3^- formation results of CeO_2-TiO_2 composite nanostructures after calcination at 673 K. It was found that CeO_2 nanoparticles and CeO_2-TiO_2 composite nanostructures have the ability to oxidize I^- to I_2 although the TiO_2 nanostructure shows little activity. The activity of the CeO_2-TiO_2 composite nanostructure reaches a maximum at CeBu/TIPT = 75/25 at 623 K.

It is known that cerium oxide shows a high oxidation ability and oxygen storage capacity, and the appearance of these functions is attributed to the following two reasons. One is the redox couple Ce^{3+}/Ce^{4+}, which shows the ability of cerium oxide to shift between CeO_2 and

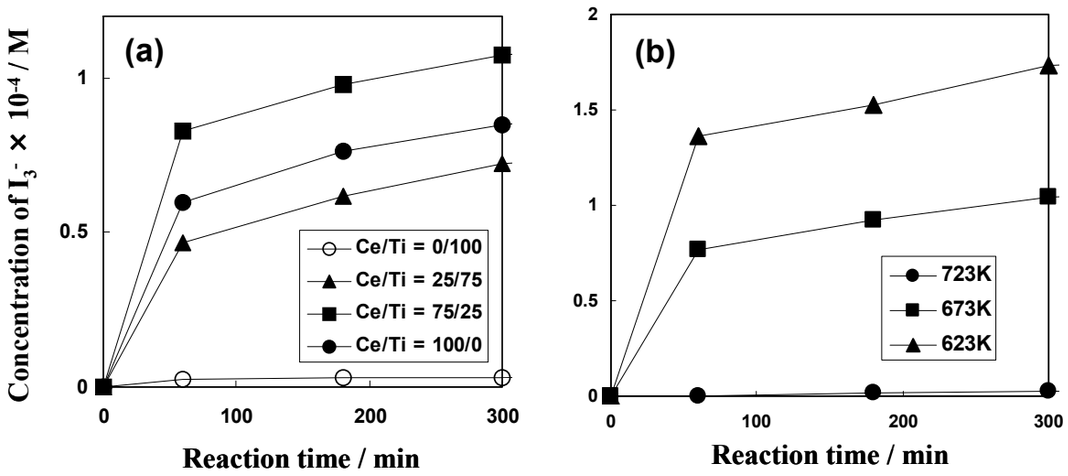

Fig. 7. The variation of concentration of I_3- with reaction time, (a) the effect of the mole ratio of CeBu/TIPT calcined at 673 K, (b) the effect of calcination temperature at the mole ratio of CeBu/TIPT = 75/25.

Ce_2O_3 under oxidizing and reducing conditions, respectively. Another is its structure: the stable structure of cerium oxide at room temperature under atmospheric pressure is the cubic fluorite structure in which oxygen ions do not have a close-packed structure. Owing to this structure, cerium oxide can easily form many oxygen vacancies while maintaining the basic crystal structure (Reddy et al., 2003). Cerium has a family of related mixed-valency binary oxides, which are anion-deficient and fluorite-related Ce_2O_{2n-2m} between Ce_2O_3 and CeO_2 at lower temperatures (Kang & Eyring, 1997). It is considered that many vacant oxygen sites exist in cerium oxide; the cerium cation (Ce^{n+}) acts as the Lewis acid site and robs the electron of I^-. Additionally, the number of Lewis acid sites could be altered by changing the composition of the CeO_2-TiO_2 composite, because mixed oxides, e.g., SiO_2-TiO_2 composites, have been frequently reported to exhibit higher catalytic activity than the pure metal oxide (Méndez-Román & Cardona-Martínez, 1998; Hu et al., 2003). As pointed out above, the uniformly mixed solution of the metal alkoxides led to homogeneously mixed composite oxides on the atomic scale in our preparation method.

We confirmed the formation and number of Lewis acid sites from the pyridine adsorption on the surface of the CeO_2-TiO_2 composite nanostructure (Nakagawa et al., 2007) as shown in Figure 8. In the results of IR spectra, two peaks at 1620 and 1350 cm^{-1} were assigned to the antisymmetric and symmetric stretching vibrations of the carboxyl group, respectively. A peak at 1595 cm^{-1} and two peaks at 1480 and 1440 cm^{-1} were observed, and these peaks were assignable to hydrogen-bonded pyridine and pyridine bonded to a Lewis site, respectively (Zaki et al., 1989, 2001). It was found that Lewis acid sites evidently exist in the CeO_2-TiO_2 composite nanostructures and these results show a good correlation between the reaction activity (Figure 7a) and the peak area as determined from the Lewis acid sites (Figure 8).

2.5 Conclusions of 2nd section

1. The preparation method of cubic CeO_2 nanoparticles using an alkoxide-primary amine surfactant in an aqueous solution was presented. In additoion, a clear potential to make

1D, 2D or 3D CeO_2 materials by assembling cubic-shape CeO_2 nanoparticle building blocks was also revealed.

2. CeO_2-TiO_2 composite nanostructures could be prepared by changing the mole ratio of cerium/titanium alkoxides. The morphology and crystalline structure of the CeO_2-TiO_2 composite nanostructures were influenced with the mole ratio of the metal alkoxides. These composite nanostructures showed effective reaction activity to oxidize I^- to I_2 because of the formation of the Lewis acid sites.

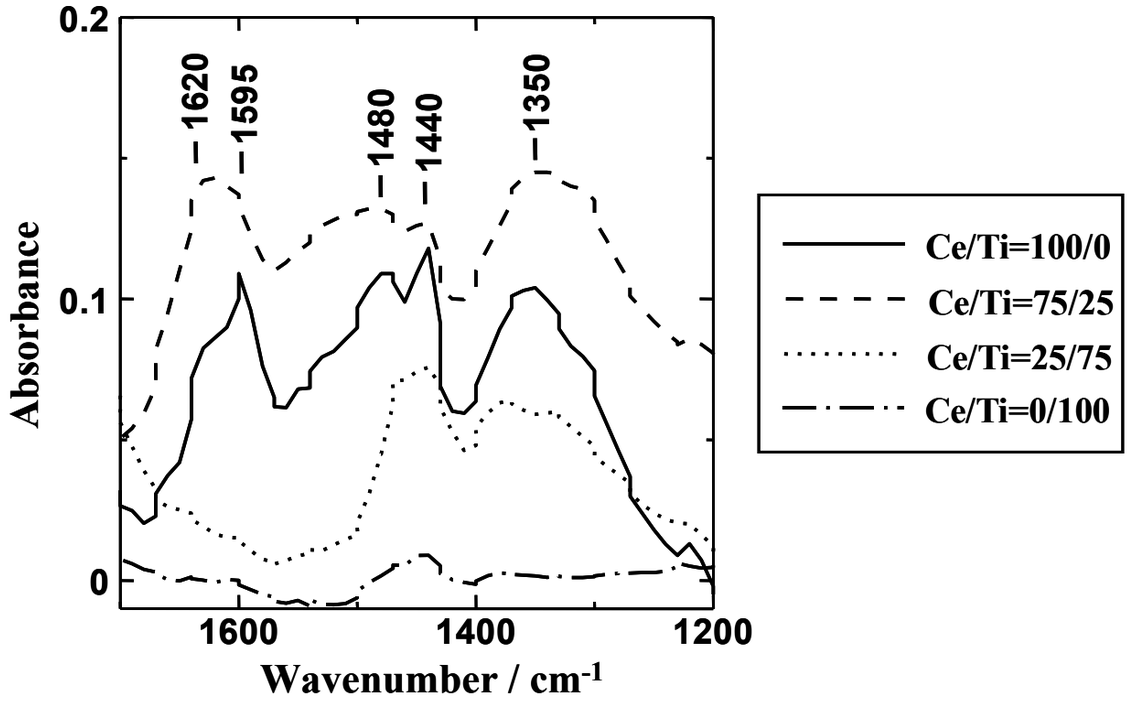

Fig. 8. Pyridine adsorption results (at room temperature) of the CeO_2-TiO_2 composite nanostructure at the different mole ratio of CeBu/TIPT calcined at 673 K.

3. 1-D TiO_2 for dye-sensitized solar cells

Dye-sensitized solar cells (DSSCs) have attracted much attention as they offer the possibility of extremely inexpensive and efficient solar energy conversion, because light from the sun is the ideal source of energy, and the supply of energy is gigantic, i.e., 3×10^{24} J/year or about 10^4 times more than what mankind consumes currently. In 1991, O'Regan and Grätzel (O'Regan & Grätzel 1991) published a remarkable report, and the Grätzel group attained 10 % efficiency in 1993 (Nazeeruddin et al. 1993). The system already reached conversion efficiency 11.5 % (Chen, C-Y. et al. 2009), and recently even 12.3 % was reported by Grätzel in Hybrid Organic Photovoltaics Conference in Valencia Spain. These conversion efficiencies exceed the level to supply electricity at the rate of home use, i.e., 10 %. Nevertheless, the energy conversion efficiency of the cells for commercial devices has not yet reached the level, which provides lower cost than that of conventional methods of electricity generation using fossil fuel. Therefore, attainment of higher efficient cells is still one of the most important challenges for the dye-sensitized solar cells.

Titania dioxide is the most promising material for the electrode of DSSCs. Many investigators have improved the anodic electrode over 10 years (Kim et al. 2009, Ito et al. 2008, Grinis et al. 2008, Hamann et al. 2008, Chen, D. et al. 2009, Miyashita et al. 2008, Wang, M. et al. 2009, Youngblood et al. 2009). One-dimensional titania nanoscale materials (1DTNM) have been investigated for attainment of highly efficient solar cells (Colodrero et al. 2009, Kar et al. 2009, Shankar et al. 2009, Wang, D. et al. 2009, Kang, T-S. et al. 2009, Kuang, D. et al. 2008, Shankar et al. 2008, Adachi et al. 2004, Jiu et al. 2006). In this section we present the clear reason for necessity of 1DTNM for attainment of higher efficient dye-sensitized solar cells through theoretical consideration and based on the experimental evidences verifying the consideration.

First we present necessity of 1DTNM theoretically based on the consideration of the electron transport processes obtained from electrochemical impedance spectroscopy (EIS), together with I−V measurement of the same cell. We present then experimentally that it is indispensable to use highly crystallized 1DTNM for attainment of higher efficient DSSCs based on the analysis of experimental results obtained by EIS and I−V measurements. Also we present that all electrodes composed of our three kinds of 1DTNM showed high light-to-electricity conversion efficiency around 9%.

3.1 Experimental procedure

In order to elucidate the relationship between the composition of titania thin film electrode and performance of the electrode, we made three kinds of electrodes, i.e., an electrode made of P-25 only, an electrode made of P-25 with polyethylene glycol (PEG) and an electrode made of network structure of titania nanowires (TNW) mixed with P-25 with PEG (TNW 28%) first. Since the electrode containing TNW was the best one, we made electrodes made of various amount of TNW mixed with the mixture of P-25 and PEG. The percentage of TNW to (TNW + P-25) in Ti atom content was varied from 0 % to 100 %. Furthermore, we made DSSCs with electrodes composed of all our three kinds of 1DTNM.

3.1.1 Synthesis of highly crystallized TiO_2 nanoscale materials

The procedure of TiO_2 single crystalline nanowires with network structure has been reported in our previous paper (Adachi et al. 2004). The synthesis procedure of highly crystallized titania nanorods has been described in our previous paper (Jiu et al. 2006). The procedure of titania nanochains is almost the same as that of titania nanorods, except usage of HCl instead of ethylenediamine (EDA) to adjust pH values to 1.3 to 5. Titania nanochains can be synthesized using P123 (triblock copolymer of (poly(ethylene oxide)$_{20}$-poly(propylene oxide) $_{70}$-poly(ethylene oxide)$_{20}$) instead of F127 (triblock copolymer of (poly(ethylene oxide)$_{106}$-poly(propylene oxide) $_{70}$-poly(ethylene oxide)$_{106}$)).

3.1.2 Preparation of titania electrods and dye-sensitized solar cells

We synthesized highly crystallized titania nanoparticles (TNP) with diameter of 3-5 nm other than 1DTNM mentioned above (Jiu et al. 2004, Jiu et al. 2007). Titania electrodes with thin film were made by applying titania samples on an electric conducting glass plate. Fluorine doped tin oxide (FTO) was used as an electric conducting oxide. Dilute solution of

TNP with diameter 3-5 nm was applied on the surface of FTO as a blocking layer. The three kinds of electrodes made of P-25 only, P-25 with PEG and titania nanowire network (TNW) mixed with P-25 with PEG were prepared by coating each gel solution containing these titania materials on the FTO glass by doctor blade method. The gel solution of P-25 only was made by dissolving P-25 powder into water. The aqueous gel solution of P-25 with PEG was made after the procedure reported by Grätzel's group (Nazeeruddin et al. 1993). The gel solution of TNW mixed with P-25 with PEG was made by mixing the gel solution of P-25 with PEG with the reaction products TNW after centrifugation and washing by 2-propanol.

The higher efficient cells constituted with 1DTNM were fabricated as follows. First, the gel solution of TNP with diameter of 3-5 nm was coated three times by doctor blade method on a FTO glass, making 3 layers of TNP. In the case of cells made of TNW, the gel solution of TNW mixed with P-25 with PEG was coated by 8-10 times. The ratio of TNW to P-25 in Ti atom content was around 0.3. In the case of cells made of titania nanorods, the reaction products after centrifugation was mixed with the two gel solutions of P-25 with PEG and the solution of TNP. The mixed gel solution was coated 7-10 times. In the case of titania nanochains, the procedure was the same as the case of titania nanorods.

After each coating, the sample was calcined at 773 K for 10 min. The last calcination was made at 773 K for 30 min. Dye was introduced to the titania thin films by soaking the film 1−3 days in 3×10^{-4} M solution of ruthenium dye in the mixed solvent of tert-butanol and acetnitryl. Cis-di(thiocyanate) bis(2,2′-bipyridyl-4,4′-di-carboxylate)-ruthenium(II) bis-tetra-butyl-ammonium (N719) (Solaronix SA) produced by Grätzel's group (Nazeeruddin et al. 1993) was used as the dye.

The DSSCs were comprised of a titania thin film electrode on a conducting glass plate, and a platinum electrode made by sputtering on the conducting glass and electrolyte between the titania thin film and the platinum. The composition of the used electrolyte was 0.1 M Guanidium thiocyanate, 0.6 M 1-butyl-3-methylimidazolium iodide, 0.03 M I_2, and 0.5 M TBP (4-tert-butyl pyridine) in the mixed solvent of acetonitrile + n-valeronitrile (volume 85 : 15).

3.1.3 Characterization of titania materials and solar cells

Characterization of the produced materials was made by X-ray diffraction (XRD) (Rigaku Goniometer PMG-A2, CN2155D2), transmission electron microscopy (TEM) (JEOL 200 CX and JEM-2100F), fast Fourier transform (FFT), selected-area electron diffraction (SAED), scanning electron microscopy (SEM) (JEOL JSM 7500FA) and isotherm of nitrogen adsorption (BEL SORP 18 PLUS). The photo-current-voltage characteristics were measured using an AM 1.5 solar simulator (YSS-E40, Yamashita Denso) and in which the light intensity is 100 mW/cm^2 calibrated with a secondary reference solar cell standardized by JET (Japan Electrical Safety & Environmental Technology Laboratories). Electron transport processes were measured by electrochemical impedance spectroscopy (EIS) (Solartron 1255B). The cell size was 0.25 cm^2.

3.2 Necessity of highly crystallized titania nanoscale materials

First, let us consider the reason why highly crystallized one-dimensional titania materials are needed. Fig. 9a shows a typical Nyquist plot obtained by EIS. Total direct current (dc)

resistance is given by the length from 0 to the point at ω=0 on the real axis as shown by Fig. 9a. This fact is confirmed later by reproduction of I−V curve using measured total dc resistances at various bias voltages as shown in Fig. 10. Total dc resistance is also obtained from the slope of the tangent line at the point of Voc. (Fig. 9b) When the total dc resistance becomes small, the slope becomes steep, and the fill factor becomes larger, resulting in a high light-to-electricity conversion efficiency. Thus, the total dc resistance should be small.

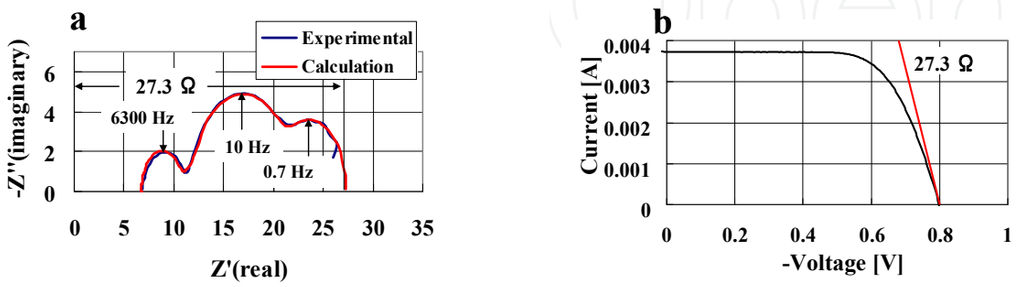

Fig. 9. (a) Typical Nyquist plot obtained by EIS, (b) I−V curve for the same cell

However, the largest arc of around 10 Hz in Fig. 9a represents the resistance of recombination reactions between electrons in the titania electrode and I_3^- ions in the electrolyte. Small total dc resistance means small resistance for recombination reactions, indicating rapid reaction rate of recombination. Thus, small total dc resistance seems an obstacle for attainment of highly efficient solar cells. But, whether electrons in the titania electrode are properly collected by the transparent conducting glass electrode or react with I_3^- ions in the electrolyte by recombination reactions is determined by the ratio of the resistance for the transport rate to the conducting glass electrode against the resistance for the recombination reactions. When the resistance for the transport rate to the conducting glass electrode is much smaller than that of the recombination reactions, almost all electrons are properly collected by the conducting glass electrode. This means that the transport rate of electrons in the titania electrode should be very rapid, indicating that we need nice titania materials with high electron transport rate, i.e., highly crystallized one-dimensional nanoscale TiO_2 materials are needed.

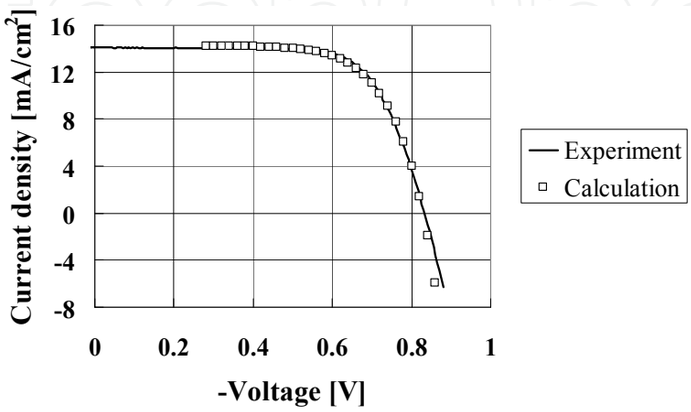

Fig. 10. Reproduction of I−V curve by total dc resistances at various bias voltages.

Solid line in Fig. 10 shows experimentally obtained I−V curve under illumination. The square keys show calculated curve based on the observed total dc resistances at various bias voltages by EIS and the following relationship between current density and voltage,

$$di = \frac{dV}{R_t} \tag{3}$$

where R_t stands for total dc resistance. The calculated curve reproduces experimentally obtained I−V curve very well, confirming that the total dc resistances can be determined accurately from Nyquist plot of EIS analysis.

3.3 Comparison of three kinds of electrodes (P-25 only, P-25 with PEG and TNW mixed with mixture of P-25 and PEG)

Fig. 11 shows I−V curves of the cells made of three kinds of electrodes, i.e., (a) P-25 only, (b) P-25 with PEG and (c) titania nanowire network (TNW) mixed with mixture of P-25 and PEG. The cell made of P-25 only showed the lowest power conversion efficiency (PCE) 4.02 %. PCE of 6.86 % was obtained for the cell made of P-25 with PEG. The highest PCE 8.64 % was obtained for the cell made of TNW mixed with mixture of P-25 and PEG, in which the percentage of titanium atoms of TNW was 28 % for the total titanium atoms, i.e., TNW + P-25. Table 1 shows the current density J_{sc}, open circuit voltage V_{oc}, fill factor FF and power conversion efficiency η of the three kinds of cells.

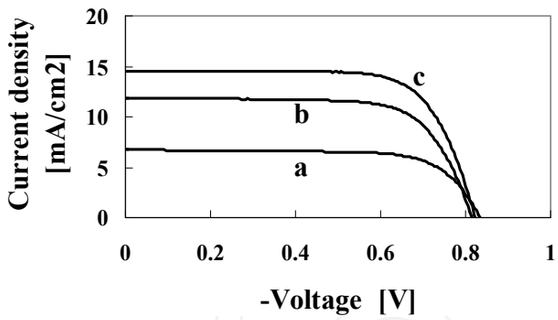

Fig. 11. I−V curves of the cells made of three kinds of electrodes, i.e., (a) P-25 only, (b) P-25 with PEG and (c) titania nanowire network (TNW) mixed with mixture of P-25 and PEG.

	J_{sc} [mA/cm2]	V_{oc} [V]	FF	η [%]
P-25	6.73	0.84	0.72	4.02
P-25 + PEG	11.38	0.83	0.73	6.86
TNW + (P-25 + PEG)	14.56	0.82	0.72	8.64

Table 1. Current density J_{sc},, open circuit voltage V_{oc}, fill factor FF and power conversion efficiency η of the three kinds of cells.

The results of incident photon to current efficiency (IPCE) for the three kinds of cells are shown in Fig. 12. IPCE of the cell made of P-25 only was lowest because of the small amount of dye adsorption. The cell made of TNW with P-25 with PEG showed highest IPCE because

of the largest amount of dye adsorption. Also IPCE in the range of 600 nm to 700 nm shows shoulder like increase because of the strong scattering of TNW.

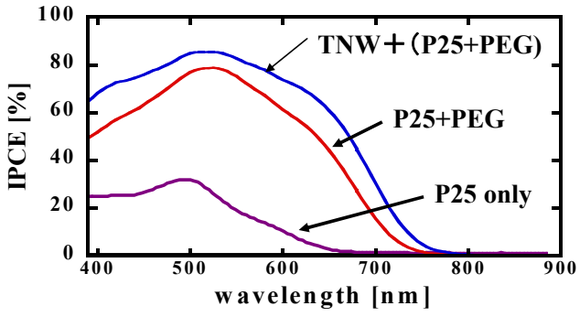

Fig. 12. Results of IPCE for three kinds of cells.

Fig. 13 shows Nyquist plots of the three kinds of cells under open circuit conditions. The total resistance of each cell was obtained as 49 Ω for P-25 only cell, 32 Ω for P-25+PEG cell and 27 Ω for TNW+(P-25+PEG) cell, respectively. Since total resistance corresponds to the slope of the tangent line at *V*oc, the slope of the tangent line in I—V curves in Fig. 11 became steeper with decreasing of the total resistance of the cell. The plotted squares in Fig. 13 represent experimental results and the solid curves show the calculated spectra from equations (4) to (7) using parameters shown in Table 2 for each cell (Adachi et al. 2006).

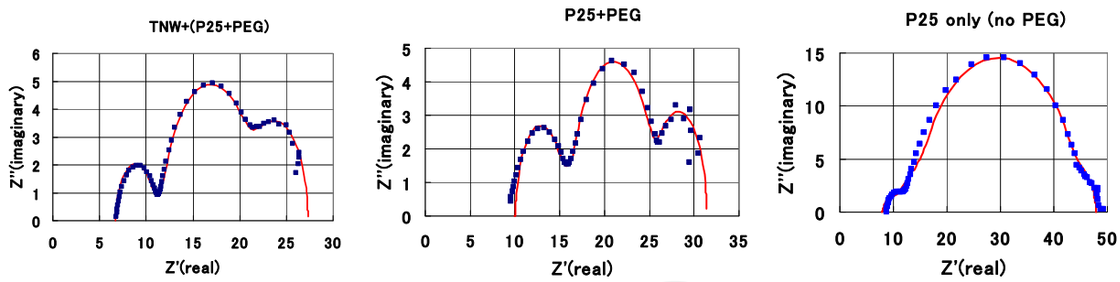

Fig. 13. Nyquist plot of three kinds of cells under open circuit conditions.

Impedance equations for electron transport processes are given as follows (Adachi et al. 2006). For the impedance concerning with titania electrode, equation (4) was derived:

$$Z = R_w \left(\frac{1}{\left(\frac{\omega_k}{\omega_d}\right)\left(1+\frac{i\omega}{\omega_k}\right)} \right)^{1/2} \coth\left[\left(\frac{\omega_k}{\omega_d}\right)\left(1+\frac{i\omega}{\omega_k}\right) \right]^{1/2} \tag{4}$$

where,

$$\omega_d = \frac{D_{eff}}{L^2},\ \omega_k = k_{eff},\ R_w = \frac{k_B T}{q^2 A n_s}\frac{L}{D_{eff}} = Con\frac{L}{D_{eff}},\ R_k = Con\frac{1}{Lk_{eff}} \tag{5}$$

For the impedance concerning with platinum electrode, equation (6) was assumed:

$$Z_{Pt} = \frac{1}{1 + i\omega r_{pt} C_{pt}} \tag{6}$$

where, r_{pt} and C_{pt} represent the resistance at the Pt surface and the capacitance at the Pt surface, respectively. For the impedance concerning with tri-iodide diffusion, finite Warburg impedance equation, i.e., equation (7) was assumed:

$$Z_N = R_{I3-} \frac{1}{\sqrt{\frac{i\omega}{\left(D_{I3-} / \delta^2\right)}}} \tanh \sqrt{\frac{i\omega}{\left(D_{I3-} / \delta^2\right)}} \tag{7}$$

The calculated solid curves in Fig. 13 agree quite well with the plotted experimental data. The characteristics shown in Table 2 are following three points which show strong tendency for the highly efficient cells. 1) The resistance for the electron transport from the titania electrode to the conducting glass electrode *R*w becomes smaller with increasing conversion efficiency. 2) The ratio of the resistance for the recombination reactions against the resistance for the transport rate to the conducting glass electrode (*R*k/*R*w) becomes large, and the rate constant of recombination reactions k_{eff} becomes smaller with increasing conversion efficiency. 3) The values of Con, which represents constant inversely proportional to the

	P25 only	P25+PEG	TNW+(P25+PEG)
Con=	2.65	0.28	0.163
D_{eff}=	0.0006	0.00014	0.00008
L =	0.0042	0.0025	0.002
k_{eff}=	23	13.8	10
R_{I3-}=	5.1	7	7.5
D_{I3-}=	0.000015	0.000003	0.000005
δ =	0.005	0.005	0.005
R_{Pt}=	1.5	4.7	3.65
C_{Pt}=	0.00005	0.00007	0.00005
R_{sub}=	7.9	10	6.7
*R*k/*R*w=	1.48	1.62	2
*R*w=	14.8	5	4.08
*R*k=	27.4	8.11	8.15
n=	2.42×10^{17}	2.29×10^{18}	3.94×10^{18}

Where, Con=$k_B T/qAn$ [Ωcms^{-1}], where k_B [JK^{-1}] represents Boltzmann constant, T [K] is absolute temperature, q [C] is elementary charge, A [cm^2] is area of the cell and n [cm^{-3}] is electron density. Con: constant inversely proportional to the electron density, D_{eff} [cm^{2}s^{-1}]: diffusion coefficient of electron, L [cm]: film thickness of TiO_2 electrode, k_{eff} [s^{-1}]: reaction rat constant of recombination reactions, R_{I3-} [Ω]: diffusion resistance of I_3^-, D_{I3-} [cm^{2}s^{-1}]: diffusion coefficient of I_3^-, δ [cm]: thickness of the electrolyte phase, R_{Pt} [Ω]: resistance of Pt electrode, C_{Pt} [F]: capacity of Pt electrode, R_{sub} [Ω]: resistance of substrate, *R*w[Ω]: resistance for electron transport in the TiO_2 electrode, *R*k [Ω]: resistance for recombination reaction.

Table 2. Determined parameters concerning with electron transport by impedance spectroscopy for three kinds of cells

	*J*sc [mA/cm^2]	*V*oc [V]	*FF*	η [%]	thickness [μm]
0wt%	10.93	0.85	0.74	6.85	10
0wt%	11.82	0.82	0.71	6.87	26
0wt%	10.92	0.80	0.71	6.20	35
5wt%	11.98	0.85	0.73	7.48	19
5wt%	10.96	0.81	0.73	6.50	32
10wt%	12.84	0.84	0.73	7.87	18
10wt%	12.68	0.84	0.72	7.64	20
28wt%	14.88	0.82	0.71	8.66	24
28wt%	13.09	0.83	0.74	8.04	27
50wt%	13.39	0.85	0.71	8.02	14
50wt%	15.18	0.80	0.70	8.51	22
100wt%	11.94	0.84	0.73	7.28	5
100wt%	9.93	0.82	0.71	5.75	9
100wt%	10.16	0.84	0.70	5.97	11

Table 3. Performance of dye sensitized solar cells with various TNW content.

electron density, becomes smaller with increasing conversion efficiency, i.e., Con value increases in the order of P-25 only > (P-25+PEG) > TNW+(P-25+PEG). Therefore the electron density *n* increases with increasing conversion efficiency. So, the characteristics of highly efficient cells are high electron density, small resistance for the electron transport to the conducting glass electrode, and large ratio of the resistances *R*k/*R*w with small rate constant for recombination reactions.

3.4 Effects of content of TNW on the properties of dye-sensitized solar cells

Since the cells containing TNW gave high conversion efficiencies, we examined the effects of content of TNW in the electrode composed of TNW and P-25 upon the conversion efficiency with variation in TNW from 0 % to 100 %. Content of TNW was defined as percentage of titanium atoms of TNW in the total titanium atoms included in the titania electrode. Table 3 shows performance of DSSCs with various TNW content, i.e., J_{sc}, V_{oc}, *FF* and η, together with film thickness. Effect of TNW content on PCE is shown in Fig. 14.

PCE of the cells including TNW are higher than those cells without TNW, indicating that TNW is useful to attain high efficiency except 100% TNW case. When the film thickness of 100% TNW cells increased larger than 5 μm, peel off of the films with cracks was observed by SEM images as shown in Fig. 15, resulting that less than 6% of PCE were observed as shown in Table 3 and Fig. 14. Thus, mixing of TNW with P-25 nanoparticles is important to make robust films.

Since the amount of adsorbed dyes is another important factor to affect PCE, the amounts of adsorbed dyes for the cells with various TNW contents are shown against film thickness in Fig. 16. The amount of adsorbed dye in the cells containing TNW from 0 % to 50 % locates in the same straight line regardless of the difference in TNW contents, except 100 % TNW which shows higher adsorbed amounts.

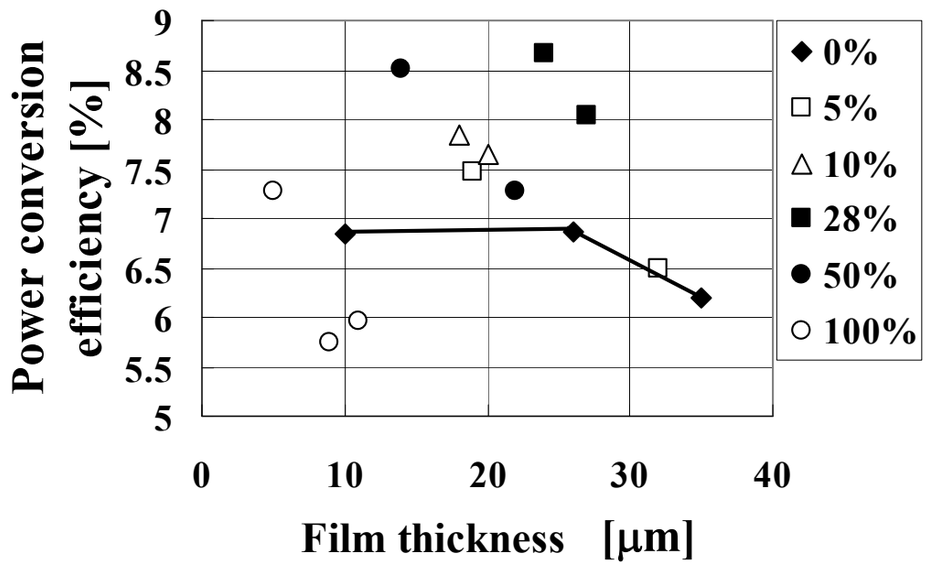

Fig. 14. Effect of content of TNW on power conversion efficiency

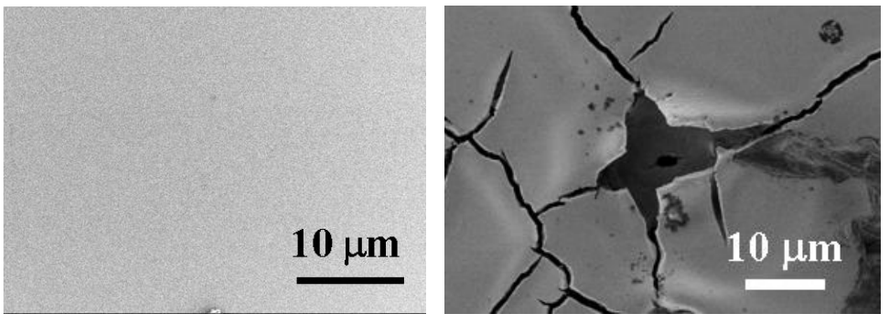

Fig. 15. Top views of 100% TNW films. Left: 5 μm, right: 11μm thickness.

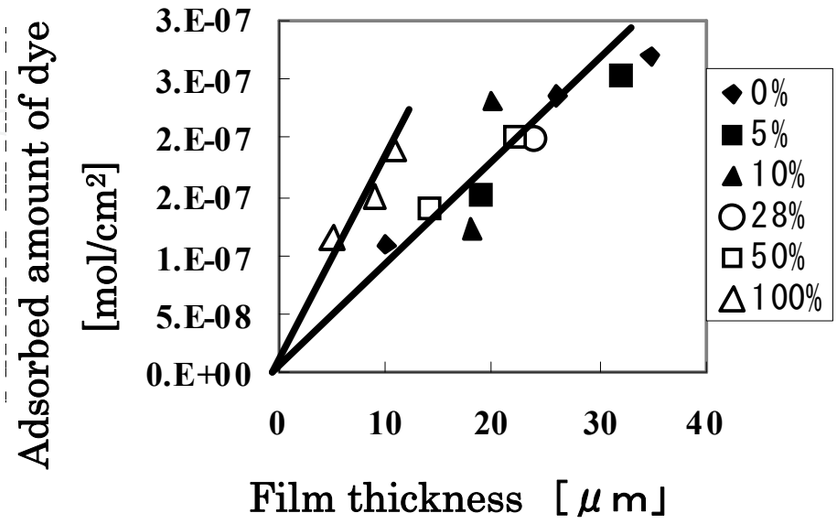

Fig. 16. Relationship between film thickness and the amount of dye.

TNW [%]	0	0	0	5	5	5	10	10	10	10
Con=	0.309	0.397	0.4	0.316	0.257	0.33	0.22	0.224	0.277	0.23
D_{eff} =	0.000038	0.000093	0.00024	0.0000747	0.000095	0.00025	0.00009	0.000085	0.00022	0.00015
L =	0.001	0.00264	0.0035	0.00191	0.00191	0.0032	0.0018	0.0018	0.002	0.002
k_{eff} =	13.8	7.67	13.8	7.67	7.67	13.8	7.67	7.67	16.3	13.8
R_{I3-} =	7.7	7	7	8	7.6	6.5	9.1	8.1	5.1	6.4
D_{I3-} =	0.00001	0.000004	0.00000295	0.000007	0.0000068	0.00000328	0.0000027	0.0000057	0.0000045	0.0000045
δ =	0.005	0.005	0.005	0.005	0.005	0.005	0.005	0.005	0.005	0.005
R_{pt} =	3.5	6.7	4.8	15	5.8	3.5	4.25	3.4	7	4.6
C_{pt} =	0.00006	0.000046	0.000055	0.0000313	0.0000675	0.00005	0.00005	0.00006	0.00004	0.000065
R_{sub} =	7.96	8.9	9.8	12	11.79	10.4	8.69	8.92	8.5	9.8
Rk/Rw=	2.75	1.74	1.42	2.67	3.4	1.77	3.62	3.42	3.37	2.72
Rw=	8.13	11.3	5.83	8.08	5.17	4.22	4.4	4.74	2.52	3.07
Rk=	22.4	19.6	8.28	21.6	17.5	7.47	15.9	16.2	8.5	8.33
n =	2.17×10^{18}	1.69×10^{18}	1.67×10^{18}	2.11×10^{18}	2.6×10^{18}	2.03×10^{18}	3.04×10^{18}	2.99×10^{18}	2.42×10^{18}	2.91×10^{18}

TNW [%]	28	28	50	50	50	50	100	100	100
Con=	0.165	0.225	0.206	0.217	0.251	0.15	0.161	0.154	0.185
D_{eff} =	0.0001	0.00012	0.00014	0.00018	0.00015	0.000104	0.000072	0.000023	0.00015
L =	0.002	0.002	0.00139	0.00139	0.0022	0.0022	0.000925	0.000505	0.0009
k_{eff} =	10	12.5	18.65	19.9	7.67	5	8	10.32	18
R_{I3-} =	5.6	5.8	6.9	6.9	9.5	11.5	14.5	13.4	11
D_{I3-} =	0.000007	0.0000055	0.000005	0.0000053	0.000003	0.0000035	0.000011	0.0000096	3.52E−06
δ =	0.005	0.005	0.005	0.005	0.005	0.005	0.005	0.005	0.005
R_{pt} =	2	2.8	3	9.85	5	3.88	4	5.8	5.7
C_{pt} =	0.0001	0.00006	0.000038	0.00006	0.0000577	0.000045	0.000052	0.00005	0.0000433
R_{sub} =	5.6	5.8	9.12	10.1	8.21	8.07	8	10.7	11
Rk/Rw=	2.5	2.4	3.89	4.68	4.04	4.3	10.5	8.74	10.3
Rw=	3.3	3.75	2.04	1.68	3.68	3.17	2.07	3.38	1.11
Rk=	8.25	9	7.94	7.84	14.9	13.6	21.8	29.5	11.4
n =	3.89×10^{18}	2.85×10^{18}	3.25×10^{18}	3.08×10^{18}	2.67×10^{18}	4.46×10^{18}	4.16×10^{18}	4.35×10^{18}	3.62×10^{18}

Table 4. Parameters determined by EIS analysis for the cells with various TNW contents.

This higher adsorption of 100 % TNW is attributed to the smaller diameter of TNW of 3-7 nm, which is much smaller than the diameter of P-25 of 23 nm. The specific surface area of P-25 and the mixture of 28 % TNW with P-25 after calcinations at 773 K for 30 min. were 45 m^2/g and 48 m^2/g, respectively. These values of specific surface area are much smaller than that of 100 % TNW which is 78 m^2/g after calcinations. This difference in specific surface area between 28 % TNW with P-25 and pure 100 % TNW corresponds well to the difference in adsorbed dye amount between from 0 % to 50 % TNW with P-25 and pure 100 % TNW. These findings suggest some interesting structural change in the surface of the mixture of TNW and P-25. However, the reason why the cells containing different TNW content from 0% to 50 % locates in the same straight line in Fig. 16 is not well understood at present.

Resistance for electron transport from titania electrode to the transparent conducting glass electrode *R*w are plotted against TNW content in Fig. 17a. *R*w values decrease steeply up to 10 % and become gradual decrease after 20 % of TNW content. This decrease indicates clearly that electron transport in the titania electrode is improved by mixing TNW with P-25 nanoparticles.

The ratios of *R*k representing the resistance for the recombination reactions between electrons in the titania electrode and I_3^- in the electrolyte to *R*w are plotted against TNW

content in Fig. 17b. The ratio of *R*k/ *R*w increases with increase in TNW content. This shows that TNW restrains the recombination reactions between electrons and I_3^- and contributes to collect electrons properly to the transparent conducting glass electrode. The findings shown in Fig. 17 a, b bring the high electron density in the titania electrode as shown in Fig. 17c.

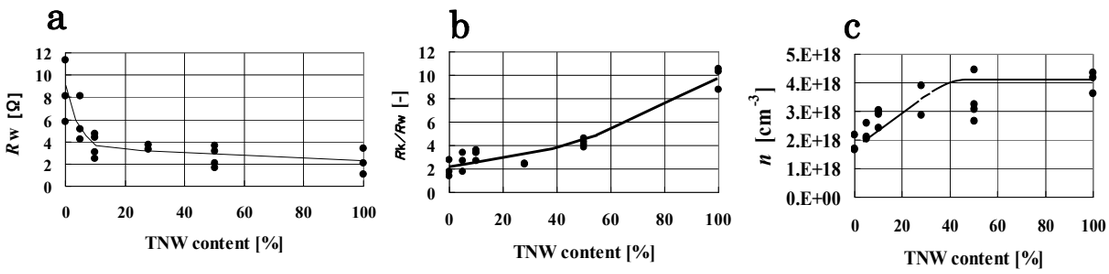

Fig. 17. a) Relationship between *R*w and TNW content, b) relationship between *R*k/*R*w and TNW cointent and c) relationship between electron density and TNW content.

Thus, the conclusion deduced from the experiments of three kinds of cells, i.e., small resistance for the electron transport to the conducting glass electrode, large value of resistance ratio *R*k/*R*w, and high electron density in the titania electrode as the characteristics of highly efficient cells, was confirmed again by the experiments of variation in TNW content.

3.5 Some examples of our highly crystallized one-dimensional TiO_2 nanoscale materials for fabricating highly efficient dye-sensitized solar cells

We succeeded in the preparation of titania nanorods (TNR) (Jiu et al. 2006), network structure of titania nanowires (Adachi et al. 2004) and one-dimensional titania nanochains (see Fig. 18), which have been newly synthesized. We applied these materials for DSSCs.

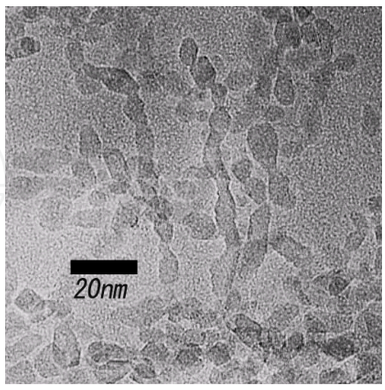

Fig. 18. TEM image of titania nanochains.

We present highly crystallized one-dimensional titania nanoscale materials are effective to attain high light-to-electricity conversion yield. As shown in our previous paper (Adachi et al. 2004), network structure of single crystal-like titania nanowires can be synthesized successfully by the oriented attachment mechanism. We attained 9.33 % conversion

efficiency with complex titania electrode made of titania nanowires and P-25. Recently, we attained the same conversion efficiency 9.33 % using different electrolyte, i.e., 0.6M 1-butyl 3-methyl imidazolium iodide, 0.1M guanidium thiocyanate, 0.05M I_2, 0.5M tert-butylpyridine in a mixture of acetonitrile and valeronitrile (85:15) for a complex titania electrode made of titania nanowires, titania nanoparticles (3-5 nm in diameter) and P-25. (Fig. 19)

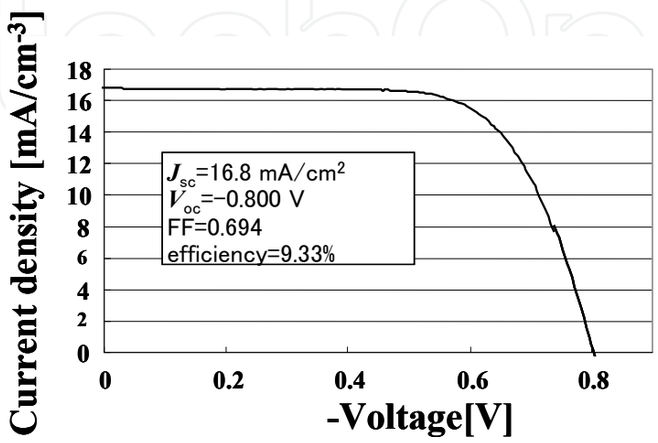

Fig. 19. I−V curve obtained for a cell with a complex electrode composed of network structure of single-crystal-like titania nanowires, titania nanoparticles and P-25

In our previous paper (Adachi et al. 2004), we used an electrolyte composed of 0.1 M of LiI, 0.6 M of1,2-dimethyl-3-n-propylimidazolium iodide, 0.05 M of I_2, 1 M of 4-tert-butylpyridine in methoxyacetonitrile and got 9.33 % conversion efficiency with short circuit current density *J*sc=19.2 mA/cm², open circuit voltage *V*oc=0.72 V and fill factor 0.675. In the recent results, *V*oc value 0.8 V is larger than that of previous one 0.72 V, because guanidium thiocyanate decreased redox potential of I^-/I_3^- in the electrolyte. Unfortunately, we got lower short circuit current density *J*sc=16.8 mA/cm² than that of our previous one, and the same efficiency was obtained.

Highly crystallized titania nanorods (TNR) have been synthesized by hydrothermal process using blockcopolymer (F127) and surfactant cetyltrimethylammonium bromide (CTAB) as a mixed template (Jiu et al. 2006). TNR with 100-300 nm in length and 20-30 nm in diameter was obtained. A high-resolution TEM (HRTEM) image of single TNR shows that titanium atoms align perfectly in titania anatase crystalline structure with no lattice defect, and the surface of TNR is facetted with the TiO_2 anatase {101} faces (Yoshida et al. 2008). The fringes are {101} planes of anatase TiO_2 with a lattice spacing of about 0.351 nm, which agrees with the value recorded in JCPDS card. The highly crystallized titania nanorods prepared successfully were used to fabricate a titania electrode of DSSCs. The complex electrodes were made by the repetitive coating-calcining process: 3 layers of titania nanoparticles (3-5 nm in diameter) were first coated on FTO conducting glass, followed by 8 layers of mixed gel composed of titania nanorods and titania nanoparticles. A high light-to-electricity conversion efficiency of 8.93 % was achieved (Yoshida et al. 2008).

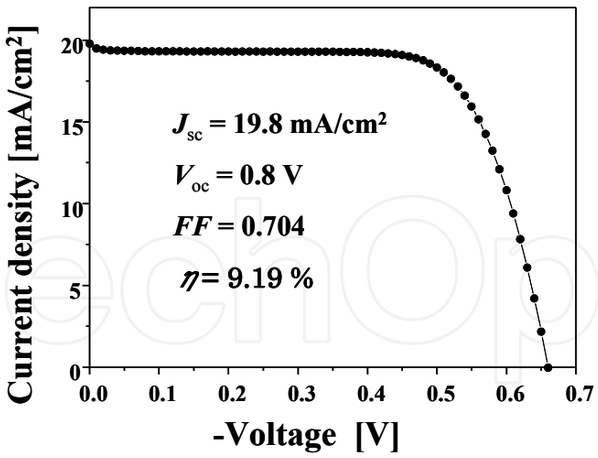

Fig. 20. I−V curve obtained for the cell composed of one-dimensional chains of titania nanoparticles mixed with fine titania nanoparticles (3 - 5 nm in diameter).

We have newly synthesized titania nanochains as shown in Fig. 18. Highly crystallized titania nanoparticles with diameter of around 10 nm combine with each other and make chains. The obtained white solid product was mixed with spherical titania nanoparticles (3-5 nm in diameter) synthesized using F127 reported in our previous paper (Jiu et al. 2004, Jiu et al. 2007) to fabricate titania film electrodes. The I−V curve of the cell is shown in Fig. 20. The obtained light-to-electricity conversion yield of the cell was 9.2%.

All three kinds of one-dimensional titania nanoscale materials mentioned above show high light-to-electricity conversion yield around 9%, suggesting strongly that highly crystallized one-dimensional titania materials are essentially important for attainment of high efficient dye-sensitized solar cells.

3.6 Conclusions of 3rd section

1. Many researchers familiar with EIS measurement know that highly efficient dye-sensitized solar cells show small total resistance of the cell, i.e., small Nyquist spectrum. They also know that largest arc of Nyquist plot represents the resistance for recombination reactions *R*k. This apparent conflict is solved clearly by theoretical consideration through recognition that the large value of the ratio *R*k/*R*w is essentially important for the highly efficient cells, and the absolute value of *R*k is not important, i.e., very small *R*w is indispensable for the highly efficient cells.
2. The experimental results of I−V and EIS measurements of the three kinds of cells made of P-25 only, P-25+PEG, and TNW+P-25+PEG and also cells made of various content of TNW with P-25+PEG clearly showed the following three points as characteristics of highly crystallized 1-dimensional titania nanoscale material TNW. 1) Resistance of electron transport in the titania electrode *R*w is small. 2) The ratio of resistance *R*k/*R*w is large. 3) Electron density *n* in the titania electrode is high.
3. All cells composed of three kinds of highly crystallized 1-dimensional titania nanoscale materials, i. e., network structure of titania nanowires, titania nanorods, and titania nanochains, show high power conversion efficiency about 9 %.

4. References

Adachi, M. Murata, Y. Takao, J. Jiu, J. Sakamoto, M. & Wang, F. (2004). Highly Efficient Dye-Sensitized Solar Cells with Titania Thin Film Electrode Composed of Network Structure of Single-Crystal-Like TiO_2 Nanowires Made by "Oriented Attachment" Mechanism. *J. Am. Chem. Soc.*, 126, pp. 14943-14949

Adachi, M. Sakamoto, M. Jiu, J. Ogata, Y. Isoda, S. (2006). Determination of Parameters of Electron Transport in Dye-Sensitized Solar Cells Using Electrochemical Impedance Spectroscopy: J. Phys. Chem. B 110, pp. 13872-13880

Aneggi, E.; de Leitenburg, C. Dolcetti, G & Trovarelli, A. (2006) Promotional effect of rare earths and transition metals in the combustion of diesel soot over CeO_2 and CeO_2–ZrO_2. *Catalysis Today*. 114, pp. 40-47.

Bekyarova, E.; Fornasiero, P.; Kaspar, J. & Graziani, M. (1998) CO oxidation on Pd/CeO_2–ZrO_2 catalysts. *Catalysis Today*. 45, pp. 179-183.

Bumajdad, A.; Zaki, M. I.; Eastoe, J. & Pasupulety, L. (2004) Microemulsion-Based Synthesis of CeO_2 Powders with High Surface Area and High-Temperature Stabilities. *Langmuir*. 20, pp. 11223-11233.

Chen, C-Y., Wang, M., Li, J-Y., Pootrakulchote, N., Alibabael, L., Ngoc-le, C-H., Decoppetr, J-D., Tsai, J-H., Grätzel, C., Wu, C-G., Zakeeruddin, M., & Grätzel, M. (2009) Highly efficient light-harvesting ruthenium sensitizer for thin-film dye-sensitized solar cells. *ACS NANO*, 3, pp. 3103-3109

Chen, D., Huang, F. Cheng, Y-B. & Caruso, R. A. (2009) Mesoporous anatase TiO_2 beads with high surface areas and controllable pore sizes: A superior candidate for high-performance dye-sensitized solar cells. *Adv. Mater.*, 21, pp. 2206-2210

Chiang, Y. M.; Lavik, E. B., Kosacki, I.; Tuller, H. L. & Ying, J. Y. (1996) Defect and transport properties of nanocrystalline CeO_{2-x}. *Appl. Phys. Lett.* 69, pp. 185-187.

Colodrero, S., Mihi, A., Häggman, L. Ocana, M. Boschloo, G. Hagfeldt, A., & Miguez, H. (2009) Porous one-dimensional photonic crystals improve the power-conversion efficiency of dye-sensitized solar cells. *Adv. Mater.*, 21, pp. 764-770

Colvin, V. L., Schlamp, M. C., & Alivisatos, A. P. (1994) Light-emitting diodes made from cadmium selenide nanocrystals and a semiconducting polymer Nature, 370, pp. 354-357.

De Faria, L. A. & Trasatti, S. (1994) The Point of Zero Charge of CeO_2. J. Colloid Interface Sci., 167, pp. 352-357.

Fuhrer, M. S., Nygard, J., Shih, L., Forero, M., Yoon, Y. -G., Mazzoni, M. S. C., Choi, H. J., Ihm, J., Louie, S. G., Zettl, A., McEuen, P. L. (2000) Crossed nanotube junctions *Science*, 288, 494-497.

Grinis, L., Dor, S., Ofir, A., & Zaban, A. (2008) Electrophoretic deposition and compression of titania nanoparticle films for dye-sensitized solar cells. *J. Photochem. Photobio. A: Chemistry*, 198, pp. 52-59

Hamann, T. W., Farha, O. K. & Hupp, J. T. (2008) Atomic layer deposition of TiO_2 on aerogel templates: New photoanodes for dye-sensitized solar cells. *J. Phys. Chem. C,* 112, pp. 19756-19764

Han, W-Q.; Wu, L. & Zhu, Y. (2005) Formation and Oxidation State of CeO_{2-x} Nanotubes. *J. Am. Chem. Soc.* 127, pp. 12814-12815.

Hirano, M.; Fukuda, Y.; Iwata, H.; Hotta, Y. & Inagaki, M. (2000) Preparation and Spherical Agglomeration of Crystalline Cerium(IV) Oxide Nanoparticles by Thermal Hydrolysis. *J. Am. Ceram. Soc.* 83, pp. 1287-1289.

Ho, C.; Yu, J. C.; Kwong, T.; Mak, A. C. & Lai, S. (2005) Morphology-Controllable Synthesis of Mesoporous CeO2 Nano- and Microstructures. *Chem. Mater.* 17, pp. 4514-4522.

Hu, S.; Willey, R. J. & Notari, B. (2003) An investigation on the catalytic properties of titania–silica materials. *J. Catal.,* 220, pp. 240-248.

Inaba, H. & Tagawa, H. (1996) Ceria-based solid electrolytes. *Solid State Ionics.,* 83, pp. 1-16.

Ito, S., Murakami, T. N., Comte, P., Liska, P., Grätzel, C., Nazeerudin, M. K. & Grätzel, M. (2008) Fabrication of thin film dye sensitized solar cells with solar to electric power conversion efficiency over 10%. *Thin Solid Film*, 516, pp. 4613-4619

Jiu, J. Isoda, S. Adachi, M. & Wang, F. (2007). Preparation of TiO2 nanocrystalline with 3-5 nm and application for dye-sensitized solar cell. *J. Photochem. Photobio. A: Cemistry*, 189, pp. 314-321

Jiu, J. Isoda, S. Wang, F. & Adachi, M. (2006). Dye-Sensitized Solar Cells Based on a Single-Crystalline TiO2 Nanorod Film. *J. Phys. Chem. B*, 110, pp. 2087-2092

Jiu, J. Wang, F., Sakamoto, M., Takao, J. & Adachi, M. (2004). Preparation of nanocrystal TiO_2 with mixed template and application for dye-sensitized solar cell. *J. Electrochem. Soc.* 151, pp. A1653-A1658

Kang, T-S., Smith, A. P., Taylor, B. E. & Durstock, M. F. (2009) Fabrication of highly-ordered TiO_2 nanotube arrays and their use in dye-sensitized solar cells. *Nano Letter*, 9, pp. 601-606

Kang, Z. C. & Eyring, L. (1997) A compositional and structural rationalization of the higher oxides of Ce, Pr, and Tb. *J. Alloys and Comp.* 249, pp. 206-212.

Kar, A., Smith, Y.R., & Subramanian, V. (2009) Improved photocatalytic degradation of textile dye using titanium dioxide nanotubes formed over titanium wires. *Environmental Sci. and Technol.*, 43, pp. 3260-3265

Kim, Y. J., Lee, M. H., Kim, H. J., Lim, G., Choi, Y. S., Park, N-G., Kim, K., & Lee, W. I. (2009) Formation of highly efficient dye-sensitized solar cells by hierarchical pore generation with nanoporous TiO_2spheres. *Adv. Mater.,* 21, pp. 3668-3673

Kuang, D., Brillet, J., Chen, P., Takata, M. Uchida, S. Miura, H., Sumioka, K., Zakeeruddin, S. M. & Grätzel, M. (2008) Application of highly ordered TiO_2 nanotube arrays in flexible dye-sensitized solar cells. *ACS Nano*, 2, pp. 1113-1116

Kuiry, S.; Patil, S.; Deshpande, S. & Seal, S. (2005) Spontaneous Self-Assembly of Cerium Oxide Nanoparticles to Nanorods through Supraaggregate Formation. *J. Phys. Chem. B,* 109, pp. 6936-6939.

Li, J. –G.; Ikegami, T.; Lee, J. –H. & Mori, T. (2001) Characterization and sintering of nanocrystalline CeO_2 powders synthesized by a mimic alkoxide method. *Acta. Mater.* 49, pp. 419-426.

Livage, J.; Henry, M. & Sanchez, C. (1988) Sol-gel chemistry of transition metal oxides. *Prog. Solid St. Chem.*, 18, pp. 259-341.

Masui, T.; Fujiwara, K.; Machida, K.; Adachi, G.; Sakata, T. & Mori, H. (1997) Characterization of Cerium(IV) Oxide Ultrafine Particles Prepared Using Reversed Micelles. *Chem. Mater.,* 9 pp. 2197-2204.

Masui, T.; Yamamoto, M.; Sakata, T.; Mori, H. & Adachi, G. (2000) Synthesis of BN-coated CeO_2 fine powder as a new UV blocking material. *J. Mater. Chem.,* 10, pp. 353-357.

Masui, T.; Hirai, H.; Imanaka, N. & Adachi, G. (2002) Synthesis of cerium oxide nanoparticles by hydrothermal crystallization with citric acid. *J. Mater. Sci. Lett.* 21, pp. 489-491.

Masui, T.; Fukuhara, K.; Imanaka, N.; Sakata, T.; Mori, H. & Adachi, G. (2002) Effects of Titanium Oxide on the Optical Properties of Cerium Oxide. *Chem. Lett.* 31, pp. 474-745.

Méndez-Román, R. & Cardona-Martínez, N. (1998) Relationship between the formation of surface species and catalyst deactivation during the gas-phase photocatalytic oxidation of toluene. *Catal. Today.*, 40, pp. 353-365.

Miyashita, M., Sunahara, K., Nishikawa, T. Uemura, Y., Koumura, N., Hara, K., Mori, A., Abe, T. Suzuki, E. & Mori, S. (2008) Interfacial electron-transfer kinetics in metal-free organic dye-sensitized solar cells: Combined effects of molecular structure of dyes and electrolytes. *J. Am. Chem. Soc*., 130, pp. 17874-17881

Morris, C. A., Anderson, M. L., Stroud, R. M., Merzbacher, C. I., & Rolison, D. R., (1999) Silica sol as a nanoglue: Flexible synthesis of composite aerogels *Science*, 284, 622-624.

Murata, Y. & Adachi, M. (2004) Formation of highly dispersed cerium oxide with cubic structure prepared alkoxide-surfactant system. *J. Mater. Sci.*, 39, 7397-7399.

Nakagawa, K.; Wang, F.; Murata, Y. & Adachi, M. (2005) Effect of Acetylacetone on Morphology and Crystalline Structure of Nanostructured TiO_2 in Titanium Alkoxide Aqueous Solution System. *Chem. Lett.* 34, pp. 736-737.

Nakagawa, K.; Murata, Y.; Kishida, M.; Adachi, M.; Hiro, M. & Susa, K. (2007) Formation and reaction activity of CeO_2 nanoparticles of cubic structure and various shaped CeO_2–TiO_2 composite nanostructures. *Mater. Chem. Phys*., 104, pp. 30-39.

Nazeeruddin, M. K., Kay, A., Rodicio, I., Humphry, B. R., Mueller, E., Liska, P., Vlachopoulous, N., & Grätzel, M. (1993) Conversion of light to electricity by cis-X_2bis(2,2′-bipyridyl-4,4′-dicarboxylate)ruthenium(II) charge-transfer sensitizers (X = Cl^-, Br^-, I^-, CN^-, and SCN^-) on nanocrystalline TiO_2 electrodes. *J. Am. Chem. Soc.*, 115, PP. 6382-6390

O'Regan, B & Grätzel, M. (1991) A low-cost, high-efficiency solar cell based on dye-sensitized colloidal TiO_2 films. *Nature*, 353, pp. 737-740

Pisarello, M. L.; Milt, V.; Peralta, M. A.; Querini, C.A. & Miró. E. E. (2002) Simultaneous removal of soot and nitrogen oxides from diesel engine exhausts. Catalysis Today. 75, pp. 456-470.

Reddy, B. M.; Khan, A.; Yamada, Y.; Kobayashi, T.; Loridant, S. & Volta, J-C. (2003) Structural Characterization of CeO_2−TiO_2 and V_2O_5/CeO_2−TiO_2 Catalysts by Raman and XPS Techniques. *J. Phys. Chem. B*, 107, pp. 5162-5167.

Reddy, B. M.; Khan, A.; Lakshmanan, P.; Aouine, M.; Loridant, S. & Volta, J-C. (2005) Structural Characterization of Nanosized CeO_2−SiO_2, CeO_2−TiO_2, and CeO_2−ZrO_2 Catalysts by XRD, Raman, and HREM Techniques. *J. Phys. Chem. B,* 109, pp. 3355-3363.

Rynkowski, J.; Farbotko, J.; Touroude, R. & Hilaire, L. (2000) Redox behaviour of ceria–titania mixed oxides. *Appl. Catal. A*, 203, pp.335-348.

Shankar, K., Basham, J. I., Allan, N. K., Varghese, O. K., Mor, G. K., Feng, X., Paulose, M. J., Seabold, A., Choi, K-S., & Grimes, C. A. (2009) Recent advances In the use of TiO_2

nanotube and nanowire arrays for oxidative photoelectrochemistry. *J. Phys. Chem. C*, 113, pp. 6327-6359

Shankar, K., Bandara, J., Paulose, M., Wietasch, H., Varghese, O. K., Mor, G. K., LaTempa, T. J., Thelakkat, M., & Grimes, C. A. (2008) Vertically aligned single crystal TiO^2 nanowire arrays grown directly on transparent conducting oxide coated glass: Synthesis details and applications. *Nano Letter*, 8, pp. 1654-1659

Sugimoto, T.; Zhou, X. & Muramatsu, A. (2003) Synthesis of uniform anatase TiO_2 nanoparticles by gel–sol method: 4. Shape control. *J. Colloid Interface Sci.*, 259, pp. 53-61.

Sun, C.; Sun, Jie.; Xiao, G.; Zhang, H.; Qiu, X.; Li, H. & Chen, L. (2006) Mesoscale Organization of Nearly Monodisperse Flowerlike Ceria Microspheres. J. Phys. Chem. B, 110, pp. 13445-13452.

Vantomme, A. ; Yuan, Z-Y. ; Du, G. & Su, B-L. (2005) Surfactant-Assisted Large-Scale Preparation of Crystalline CeO_2 Nanorods. *Langmuir*. 21, pp. 1132-1135.

Wang, D., Liu, Y., Yu, B., Zhou, F., & Liu, W. (2009) TiO_2 nanotubes with tunable morphology, diameter, and length: Synthesis and photo-electrical/catalytic performance. *Chem. Mater.*, 21, pp. 1198-1206

Wang, M., Chen, P., Humphry-Baker, R., Zakeeruddin, S. M., & Grätzel, M. (2009) The influence of charge transport and recombination on the performance of dye-sensitized solar cells. *ChemPhysChem*, 10, pp. 290-299

Wu, N-C.; Shi, E-W.; Zheng, Y-Q. & Li, W-J. (2002) Effect of pH of Medium on Hydrothermal Synthesis of Nanocrystalline Cerium(IV) Oxide Powders. *J. Am. Ceram. Soc.* 85, pp. 2462-2468.

Yoshida, K. Jiu, J. Nagamatsu, D. Nemoto, T. Kurata, H. Adachi, M. & Isoda, S. (2008). Structure of TiO2 Nanorods Formed with Doiuble Surfactants, Molecular Crystals and Liquid Crystals. 491, pp. 14-20

Youngblood, J. W., Lee, S-H. A., Kobayashi, Y., Hernandez-Pagan, E. A., Hoertz, P. G., Moor, T. A. Moor, A. L., Gust, D., & Mallouk, T. E. (2009) Photoassisted overall water splitting in a visible light-absorbing dye-sensitized photoelectrochemical cell. *J. Am. Chem. Soc.*, 131, pp. 926-927

Zaki, M. I.; M Hussein, G. A.; Mansour, S. A. A. & El-Ammawy, H. A. (1989) Adsorption and surface reactions of pyridine on pure and doped ceria catalysts as studied by infrared spectroscopy. *J. Mol. Catal.* 51, pp. 209-220.

Zaki, M. I.; Hasan, M. A. & Pasupulety, L. (2001) Surface Reactions of Acetone on Al_2O_3, TiO_2, ZrO_2, and CeO_2: IR Spectroscopic Assessment of Impacts of the Surface Acid−Base Properties. *Langmuir.*, 17, pp. 768-774.

Zhou, X. -D.; Huebner, W. & Anderson, H. U. (2003) Processing of Nanometer-Scale CeO_2 Particles. *Chem. Mater.* 15, pp. 378-382.

Zhou, K.; Wang, X.; Peng, Q. & Li, Y. (2005) Enhanced catalytic activity of ceria nanorods from well-defined reactive crystal planes. *J. Catal.* 229, pp. 206-212.

Zhong, L-S.; Hu, J-S.; Cao, A-M.; Liu, Q.; Song, W-G.; & Wan, L-J. (2007) 3D Flowerlike Ceria Micro/Nanocomposite Structure and Its Application for Water Treatment and CO Removal. *Chem. Mater.* 19, pp. 1648-1655.

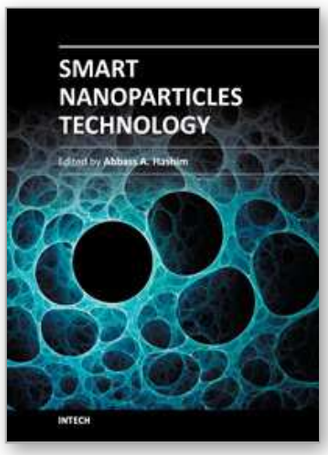

Smart Nanoparticles Technology

Edited by Dr. Abbass Hashim

ISBN 978-953-51-0500-8
Hard cover, 576 pages
Publisher InTech
Published online 18, April, 2012
Published in print edition April, 2012

In the last few years, Nanoparticles and their applications dramatically diverted science in the direction of brand new philosophy. The properties of many conventional materials changed when formed from nanoparticles. Nanoparticles have a greater surface area per weight than larger particles which causes them to be more reactive and effective than other molecules. In this book, we (InTech publisher, editor and authors) have invested a lot of effort to include 25 most advanced technology chapters. The book is organised into three well-heeled parts. We would like to invite all Nanotechnology scientists to read and share the knowledge and contents of this book.

How to reference

In order to correctly reference this scholarly work, feel free to copy and paste the following:

Motonari Adachi, Keizo Nakagawa, Yusuke Murata, Masahiro Kishida, Masahiko Hiro, Kenzo Susa, Jun Adachi, Jinting Jiu and Fumio Uchida (2012). Utilization of Nanoparticles Produced by Aqueous-Solution Methods – Formation of Acid Sites on CeO2-TiO2 Composite and 1-D TiO2 for Dye-Sensitized Solar Cells, Smart Nanoparticles Technology, Dr. Abbass Hashim (Ed.), ISBN: 978-953-51-0500-8, InTech, Available from: http://www.intechopen.com/books/smart-nanoparticles-technology/utilization-of-nanoparticles-produced-by-aqueous-solution-methods-formation-of-acid-sites-on-ceo2-ti

INTECH
open science | open minds

InTech Europe
University Campus STeP Ri
Slavka Krautzeka 83/A
51000 Rijeka, Croatia
Phone: +385 (51) 770 447
Fax: +385 (51) 686 166
www.intechopen.com

InTech China
Unit 405, Office Block, Hotel Equatorial Shanghai
No.65, Yan An Road (West), Shanghai, 200040, China
中国上海市延安西路65号上海国际贵都大饭店办公楼405单元
Phone: +86-21-62489820
Fax: +86-21-62489821

IntechOpen